A frequency-modulated continuous-wave reflectometer for the Lithium Tokamak Experiment

S. Kubota,[1, a] R. Majeski,[2] W. A. Peebles,[1] R. E. Bell,[2] D. P. Boyle,[2] R. Kaita,[2] T. Kozub,[2] M. Lucia,[2]
E. Merino,[2] X. V. Nguyen,[1] T. L. Rhodes,[1] and J. C. Schmitt[2]
[1] *Department of Physics and Astronomy, University of California, Los Angeles, CA 90095*
[2] *Princeton Plasma Physics Laboratory, Princeton, NJ 08543*

The FM-CW (frequency-modulated continuous-wave) reflectometer on the LTX (Lithium Tokamak eXperiment) and the method for determining electron density profiles is described. The diagnostic uses a frequency range of 13.1−33.5 GHz, for covering a density range of $0.21-1.4\times10^{13}$ cm^{-3} (in O-mode polarization) with a time resolution down to 8 μs. The design of the diagnostic incorporates the concept of an "optimized" source frequency sweep, which minimizes the large variation in the intermediate frequency signal due to a long dispersive transmission line. The quality of the raw data is dictated by the tuning characteristics of the microwave sources, as well as the group delay ripple in the transmission lines, which can generate higher-order nonlinearities in the frequency sweep. Both effects are evaluated for our diagnostic and best practices are presented for minimizing "artifacts" generated in the signals. The quality of the reconstructed profiles is also improved using two additional data analysis methods. First, the reflectometer data is processed as a radar image, where clutter due to echos from the wall and backscattering from density fluctuations can be easily identified and removed. Second, a weighed least-squares lamination algorithm POLAN (POLynomial ANalysis) is used to reconstruct the electron density profile. Examples of density profiles in LTX are presented, along with comparisons to measurements from the Thomson scattering and the λ=2 mm interferometer diagnostics.

I. INTRODUCTION

Reflectometry and scattering diagnostics using microwave and millimeter-wave frequencies, can provide a powerful set of tools for measuring electron density profiles and fluctuations in fusion plasma devices.[1] In particular, frequency-modulated continuous-wave (FM-CW) reflectometry is a well-established method for measuring electron density profiles with high spatial and temporal resolution.[2] FM-CW and pulsed radar reflectometry have a long history in ionospheric sounding measurements.[3] For laboratory plasmas,[4] the frequency of a broadband microwave or millimeter-wave source is swept as a function of time, and the round-trip propagation delay from the plasma edge to the cutoff density is inverted to obtain the electron density profile. The basic principles of the technique are encompassed in the following equation for the roundtrip time-of-flight (TOF) of an electromagnetic wave at frequency f:[5]

$$\tau_{\rm p}(f) = \frac{2}{c}\int_{R_a}^{R_{\rm c}(f)} \mu_{\rm g}(f,r)dr, \tag{1}$$

where R_a is the radius of the plasma edge, $R_{\rm c}(f)$ is the radius of the wave cutoff, and the group index of refraction $\mu_{\rm g}(f,r)$ has the general form

$$\mu_{\rm g}(f,r) = \mu(f,r) + f\frac{\partial\mu(f,r)}{\partial f}. \tag{2}$$

Here the index of refraction $\mu(f,r)$ for perpendicular propagation ($\mathbf{k}\perp\mathbf{B}_0$) has the following dependence on the wave polarization for electron waves:[6]

$$\mu^2(f,r) = \begin{cases} 1-\dfrac{f_{\rm pe}^2(r)}{f^2} & \text{O-mode} \\ 1-\dfrac{f_{\rm pe}^2(r)(f^2-f_{\rm pe}^2(r))}{f^2(f^2-f_{\rm ce}^2(r)-f_{\rm pe}^2(r))} & \text{X-mode,} \end{cases} \tag{3}$$

where the plasma frequency $f_{\rm pe}(r) = \sqrt{e^2 n_{\rm e}(r)/m_{\rm e}\pi}$ and electron cyclotron frequency $f_{\rm ce}(r) = eB_0(r)/2\pi m_{\rm e}c$ are dependent on the radial profile of the electron density $n_{\rm e}(r)$ and the magnetic field $B_0(r)$. For FM-CW sources, the TOF is proportional to the beat or intermediate frequency ($f_{\rm IF}$) generated by the mixing of waves traveling along the probe (with plasma) and reference (without plasma) paths. Typically $\tau_{\rm p}(f)$ and $B_0(r)$ are known, while $n_{\rm e}(r)$ is the quantity to be determined.

Several issues must be considered for the accurate reconstruction of electron density profiles. The frequency sweep should be faster than the motion of the density profiles (and fluctuations) that are to be measured.[7] In the case of broadband frequency sources such as HTOs (hyperabrupt veractor-tuned oscillators) used in this work, the source frequency is controlled by a tuning voltage signal from a waveform generator. For higher sweep rates, "artifacts" in the intermediate frequency signal may be generated due to higher-order nonlinearities in the source frequency sweep.[8] Strong reflections from false targets (backscattering due to fluctuations away from the cutoff layer) can degrade the quality of the reconstructed density profile, and these should be removed from the raw data. Finally, regularization is required in the inversion process to generate useful density profiles from noisy $\tau_{\rm p}(f)$ data. A common method is to smooth $\tau_{\rm p}(f)$ by using a moving average filter and/or averaging data from

---

[a] Electronic mail: skubota@ucla.edu

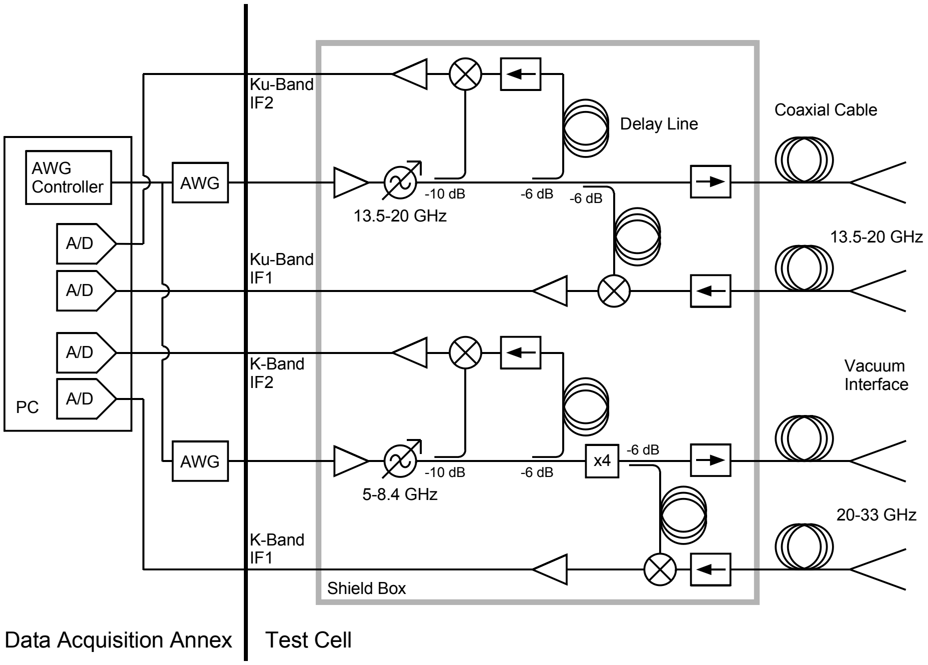

FIG. 1. Simplified diagram of the microwave circuit. The transmission line from the shield box to the machine consists of coaxial cable and the vacuum interface shown in Fig. 2.

multiple sweeps, however the time and spatial resolutions of the measurement are degraded.

The main goal of this paper is to describe the hardware capabilities and initial results of the FM-CW reflectometer fabricated for generating time- and space-resolved electron density profiles for the Lithium Tokamak eXperiment (LTX).[9] LTX is a low-aspect ratio spherical torus designed with a major radius R_0=40 cm, minor radius a=26 cm, and plasma elongation κ=1.5. The toroidal field on-axis is B_0=1.7 kG, while peak plasma currents have reached I_p=75 kA. Durations of the current flattop have exceeded 25 ms with a reduced maximum current of I_p=30 kA. Line-averaged densities up to 2×10^{13} cm^{-3} and central electron temperatures up to 200 eV have been measured. The vacuum vessel contains a close fitting shell (1.5 mm of stainless steel explosively bonded to 1 cm of copper) on which lithium coatings are evaporated. Heating the shell allows LTX to operate with liquid lithium wall coatings. The LTX reflectometer utilizes microwave hardware from the NSTX core FM-CW reflectometer.[10] The hardware components are described in Sec. II, while the initial measurement results are presented in Sec. V. Future upgrades to the system are discussed in Sec. VI.

A second goal of this paper is to introduce techniques that are used to address some of the issues (raised earlier in this section) that limit FM-CW reflectometer performance. A critical component of all FM-CW systems is the source frequency sweep, which directly influences the quality of the measured data. In Sec. III, we introduce the "optimized" source frequency sweep (defined in Sec. III.C), which minimizes variations in f_{IF} due to higher-order nonlinearities in the frequency sweep. In Sec. IV, two method for vastly improving the quality of the reconstructed density profiles are introduced. First, the radar image of the raw data is used to eliminate reflections from false targets. Second, this data is inverted using a weighted least-squares lamination algorithm POLAN (POLynomial ANalysis), which is particularly robust against noisy data.

II. DIAGNOSTIC DESCRIPTION

A. Microwave Hardware and Data Acquisition

The microwave hardware described here was previously used on NSTX, with several modifications made for LTX. A schematic of the microwave circuit is shown in Fig. 1. The launch and receive antennas are separate (bistatic) and two frequency bands 13.1−20.5 GHz (K$_u$-band) and 19.5−33.5 GHz (K-band) are used to cover the density range of 0.22−1.4 × 10^{13} cm^{-3} in O-mode. The frequency sources are hyperabruct varactor-tuned oscillators (HTOs) which are swept using Agilent 33220A arbitrary waveform generators (AWGs). The full frequency band can be swept in 3–4 μs (sweep time interval). Figure 1 reveals that for each frequency band there are two sub-circuits: one mixer (output IF1) has a reference path that contains the plasma, while the other mixer (output IF2) has a reference path that consists of a fixed length of coaxial cable. The signal IF2 is used to determine the level of timing jitter between the arbitrary waveform generator and the digitizer (see below).

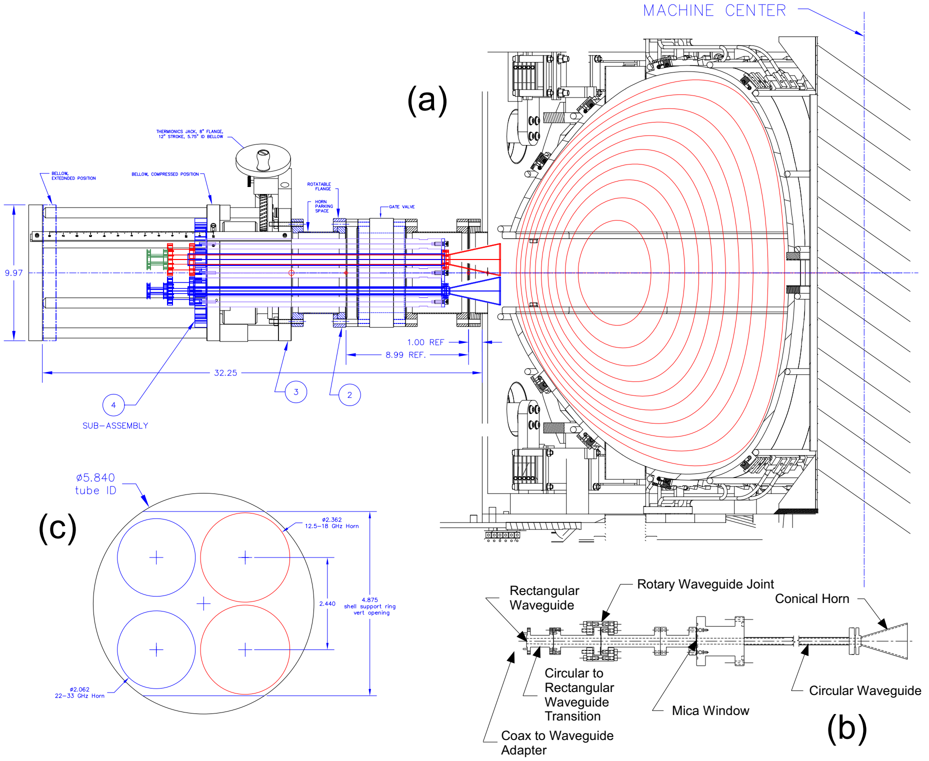

FIG. 2. Reflectometer vacuum interface on LTX. (a) shows a side view of the jacking stage and bellows with the antennas fully inserted, (b) shows the rotatary joints attached to the waveguide ends, and (c) shows the orientation of the antenna arrays.

The data acquisition consists of a GaGe Razor CompuScope 1222, which has 128 MSa of storage and can digitize dual channels at 200 MSa/s (100 MSa/s sampling rate is used here). Triggers are generated by a National Instruments PCI-6602 counter/timer cards. Each trigger to the AWG initiates a frequency up-sweep, while a delayed trigger to the digitizer in burst mode starts the data acquisition. With a sweep interval of ∼3.7 μs (and a similar record length), this sequence can be repeated every 8 μs and is limited by the dead time of the digitizer. The timing jitter between the AWG and digitizer is typcially ±13 ns, which introduces negligible errors for density profile measurements. LabVIEW software is used to control both the data acquisition and the triggering hardware, as well as to communicate with the AWGs.

B. Vacuum Vessel Interface

The LTX plasma is enclosed by four quadrants of a close fitting shell, and the plasma is accessed between the poloidal gap at the outboard midplane between upper and lower sections. The antennas are inserted as close to the plasma as possible for two reasons: 1) to provide a better edge constraint for the density profile inversion, and 2) to avoid reflections from the outer surface of the shell. The reflectometer antennas utilize an 8 inch diameter port at the LTX midplane (see Fig. 2(a)). Four antennas are mounted at the end of 20.5 inch lengths of circular waveguides (inner diameters of 0.677 inch for K_u-band, 0.375 inch for K-band) which are attached to a rotatable flange. The jacking stage and bellows construction allows the horns to be retracted beyond a gate valve. When fully inserted, the horns are positioned to within 0.5 inch of the outer edge of the shell.

A pair of bistatic antenna arrays are used for launching and receiving the electromagnetic waves. The end flange on which the waveguides are mounted is rotatable, and Fig. 2(b) shows the orientation of the antennas as they are currently installed. The vertical orientation of the antenna arrays assures that both reflectometer systems will view similar density profiles, since toroidal asymmetries in the plasma shape are assumed to be much smaller than poloidal or vertical asymmetries. The spot size (FWHM) of the beam in vacuum at mid-radius (R = 52.5 cm or 14.3 cm from the antennas) in the E- and H-planes is 4.6 and 5.7 cm for the K_u-band (at 16.8 GHz), and 3.3 and 4.1 cm for the K-band (at 26 GHz).

A mechanical rotary joint, along with the combination of a circular-to-rectangular waveguide transition and a coaxial-to-rectangular adapter, determines the polarization of the launched and received waves (Fig. 2(c)). The waveguide components are attached to the microwave shield box by 60 inches of coaxial cable. The group delay due to these cables are offset by a similar length of coaxial delay line along the reference path inside the shield box. The circular waveguide introduces signficant dispersion of the waves along the probe path, which is compensated by tailoring the source frequency sweep (Sec. III).

III. SOURCE FREQUENCY SWEEP

Aside from the microwave hardware itself, the source frequency sweep is the most critical component of the FM-CW diagostic. Section III.A outlines the connection between the signals and the quantity of interest $\tau_{\rm p}(f)$. The optimized frequency sweep is dependent group delay characteristics of the reflectometer system, hence these are described in Sec. III.B. The optimized frequency sweep itself is defined in Sec. III.C, while the consequences of higher-order nonlinearities in $f(t)$, due in part to group delay ripple, are described in Sec. III.D.

A. Connection Between Reflectometer Signals and $\tau_{\rm p}(f)$

Using standard mixer terminology, the intermediate frequency (IF) signal at the mixer output results from the combination of electromagnetic waves traveling along the reference or local oscillator (LO) path, and the probe or radio frequency (RF) path. The time delay $\tau_{\rm LO}$ along the a length of transmission line $\ell_{\rm LO,coax}$ is assumed to be non-dispersive (coaxial), while the RF path is composed of both dispersive (waveguide) and non-dispersive (coaxial and vacuum) sections. We refer to the path length in the respective sections as $\ell_{\rm wg}$, $\ell_{\rm RF,coax}$ and $\ell_{\rm vac}$, and the corresponding group velocities as $v_{\rm g,wg}(f)$, $v_{\rm g,coax}$ and c (speed of light in vacuum).

For an electromagnetic wave with frequency f, the difference in time delay along the probe path is expressed as

$$\tau_{\rm RF}(f) = \underbrace{\tau_{\rm wg}(f) + \tau_{\rm coax} + \tau_{\rm vac}}_{\equiv\, \tau_{\rm RF,edge}(f)} + \tau_{\rm p}(f) \tag{4}$$

$$\tau_{\rm RF,edge}(f) = \frac{\ell_{\rm wg}}{v_{\rm g,wg}(f)} + \frac{\ell_{\rm RF,coax}}{v_{\rm g,coax}} + \frac{\ell_{\rm vac}}{c}. \tag{5}$$

For a time-dependent frequency sweep $f(t)$, the frequency of the mixer IF signal is related to $\tau_{\rm p}(f)$ by the equation

$$\tau_{\rm p}(f(t)) \simeq \frac{1}{\gamma(t)} \underbrace{\left[f_{\rm IF}(t) - f_{\rm IF,edge}(t)\right]}_{\equiv\, \Delta f_{\rm IF}(t)}, \tag{6}$$

where

$$f_{\rm IF}(t) = f(t - \tau_{\rm LO})) - f(t - \tau_{\rm RF}(f(t))) \tag{7}$$

$$f_{\rm IF,edge}(t) = f(t - \tau_{\rm LO})) - f(t - \tau_{\rm RF,edge}(f(t))) \tag{8}$$

represent the time-dependent instantaneous frequencies of IF signals with a plasma target, and a mirror target placed at the plasma edge, respectively. The relations between these quantitiess are shown graphically in Fig. 3.

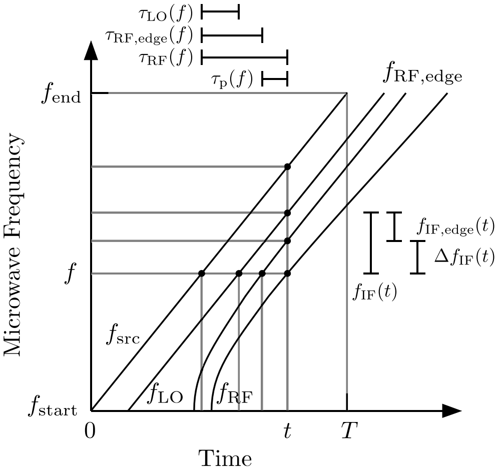

FIG. 3. Plot of the curves $f(t){=}f_{\rm src}(t)$, $f_{\rm LO}(t)$, $f_{\rm RF,edge}(t)$ and $f_{\rm RF}(t)$. Also shown graphically are the quantities $\tau_{\rm RF}$, $\tau_{\rm RF,edge}$, $\tau_{\rm LO}$ and $\tau_{\rm p}$ for a given f, and $f_{\rm IF}$, $f_{\rm IF,edge}$, and $\Delta f_{\rm IF}$ for a given t.

The source frequency $f(t)$ and sweep rate $\gamma(t)$ are defined by

$$f(t) = f_{\rm start} + \int_0^t \gamma(t')dt', \quad \gamma(t) \equiv \frac{df(t)}{dt}. \tag{9}$$

The approximation in Eq. 6 holds provided that the following condition applies:

$$\left|\gamma(t)\left[\frac{\partial \tau_{\rm wg}(f(t))}{\partial f} + \frac{\partial \tau_{\rm plasma}(f(t))}{\partial f}\right]\right| \ll 1, \tag{10}$$

where $\gamma(t)$ is an externally adjustable parameter and $(\partial\tau_{\rm plasma}/\partial f <)\partial\tau_{\rm wg}/\partial f$ is an intrinsic property of the system. Equation 10 is important for ultrafast sweeps[11] where the value of $\gamma(t)$ becomes large.

B. Group Delay Characterics of the System

Both the static f–$V_{\rm t}$ characterization of the source, as well as the phase (or equivalently group) delay characterization of the reflectometer system, were performed simultaneously by stepping the tuning voltage (1 mV steps), and recording both the source frequency (EIP 548A Microwave Frequency Counter) and the output from the mixer IF port. A flat metal plate placed at $\ell_{\rm ref}/2 = 20$ cm from the antennas was used as the reference target. The phase of the IF signal $\phi_{\rm IF,ref}$ is related to the time delay difference between the RF and LO paths:

$$\begin{aligned}\tau_{\rm IF,ref}(f) &= \tau_{\rm RF,ref}(f) - \tau_{\rm LO} \\ &= \frac{\ell_{\rm wg}}{v_{\rm g,wg}(f)} + \frac{\ell_{\rm RF,coax} - \ell_{\rm LO,coax}}{v_{\rm g,coax}} + \frac{\ell_{\rm ref}}{c}\end{aligned} \tag{11}$$

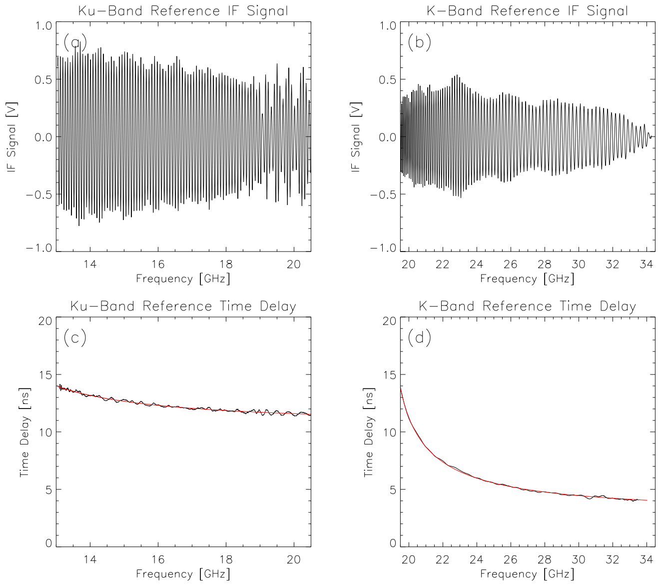

FIG. 4. Top row shows the IF signal for (a) the K_u-band and (b) the K-band systems. Bottom row shows the time delay difference between LO and RF paths from a reference target, $\tau_{\mathrm{IF,ref}}(f)$, for (c) the K_u-band and (d) the K-band systems. Overlayed in red are the best fits to Eq. 11.

through the relation

$$\frac{1}{2\pi}\frac{d\phi_{\mathrm{IF,ref}}(f)}{df} = \tau_{\mathrm{IF,ref}}(f). \tag{12}$$

The nominal group velocity of the coaxial cable is $0.84c$, while that for the circular waveguide section can be approximated by[12]

$$\frac{v_{\mathrm{g,wg}}(f)}{c} = \sqrt{1-\left(\frac{k_{\mathrm{c}}}{k_0}\right)^2}, \tag{13}$$

where $k_0 = \omega/c$ is the vacuum wavenumber and $k_{\mathrm{c}} = 1.841/a$ is the cutoff wavenumber of the waveguide. Here a is the waveguide radius ($a = 0.860$ cm for K_{u}-band, 0.476 cm for K-band) and the TE_{11} mode is assumed.

Figures 4(a) and 4(b) show the K_{u}-band and K-band IF signals, respectively, due to reflection from the reference target. Figures 4(c) and 4(d) show the time delay difference $\tau_{\mathrm{IF,ref}}$ as a function of frequency, as well as the best fit curve to the data using Eq. 11. This analysis yields values of $\ell_{\mathrm{wg}} = 159.3$ cm and 154.4 cm, and $\ell_{\mathrm{RF,coax}} - \ell_{\mathrm{LO,coax}} = 102.6$ cm and -85.8 cm, respectively, for the K_{u}- and K-bands. The above information is used in Sec. III.C to generate the tuning voltage waveforms for the frequency sweeps. In addition, the results in Figs. 4(c) and 4(d) show that $\gamma(t)\partial\tau_{\mathrm{wg}}/\partial f < 0.011$ for the K_{u}- and K-bands, respectively, which indicates that Eq. 10 is satisfied and that Eq. 6 is still a valid estimate for $\tau_{\mathrm{p}}(f)$.

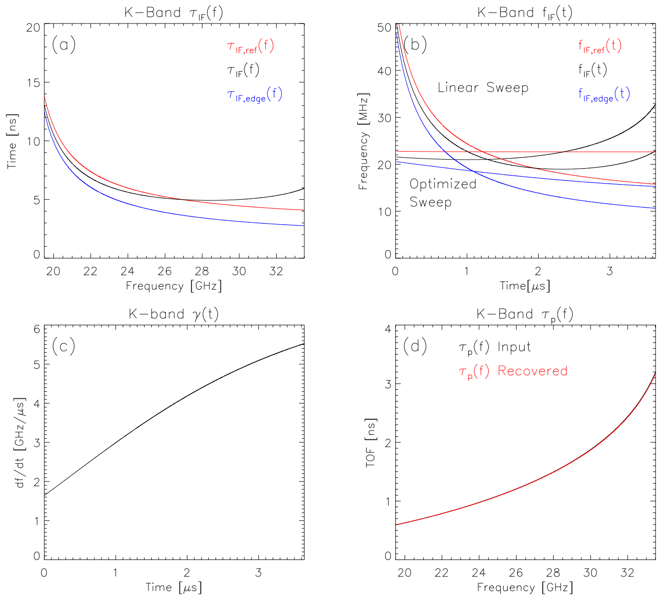

FIG. 5. (a) The K-band delay times $\tau_{\mathrm{IF,ref}}$ (red), $\tau_{\mathrm{IF,edge}}$ (blue) and $\tau_{\mathrm{IF,plasma}}$ (black). (b) The corresponding IF curves $f_{\mathrm{IF,ref}}$ (red), $f_{\mathrm{IF,edge}}$ (blue) and $f_{\mathrm{IF,plasma}}$ (black) for linear and optimized sweeps. (c) The optimized frequency sweep rate $\gamma(t)$. (d) The recovered $\tau_{\mathrm{plasma}}(f)$ (red) curve overlayed atop the input $\tau_{\mathrm{plasma}}(f)$ (black) curve, for the optimized frequency sweep and using the approximation in Eq. 6. Here we used $\ell_{\mathrm{vac}} = 0$ and $\ell_{\mathrm{ref}}/2 = 20$ cm.

C. Optimized Source Frequency Sweep

In most broadband FM-CW sytems, the tuning voltage waveform is predistorted in an attempt to generate a frequency sweep that is linear in time ($\gamma =$ constant). In this case, any variation in $f_{\mathrm{IF}}(t)$ is due only to the dispersive portion of the transmission line and the path through the plasma.

The effect of a linear source frequency sweep on the IF signals is modeled for the K-band system using the experimental fit of $\tau_{\mathrm{IF,ref}}$ to Eq. 11 (see Fig. 5(a)). Also shown are the time delays

$$\tau_{\mathrm{IF,edge}}(f) = \tau_{\mathrm{RF,edge}}(f) - \tau_{\mathrm{LO}} \tag{14}$$

$$\tau_{\mathrm{IF}}(f) = \tau_{\mathrm{RF}}(f) - \tau_{\mathrm{LO}}, \tag{15}$$

with $\ell_{\mathrm{vac}} = 0$ and $\ell_{\mathrm{ref}}/2 = 20$ cm. Here $\tau_{\mathrm{p}}(f)$ was calculated for a parabolic density profile with peak density $n_{e0} = 1.5\times10^{13}$ cm^{-3} and minor radius $r_a = 25$ cm. Figure 5(b) shows the corresponding values of $f_{\mathrm{IF,ref}}(t)$, $f_{\mathrm{IF,edge}}(t)$ and $f_{\mathrm{IF}}(t)$, where the variation due to the transmission line dispersion is several times the size of the contribution from the plasma path. Signal processing (e.g. a moving window FFT) will better extract $\tau_{\mathrm{p}}(f)$ from the IF signal if systematic variations in $f_{\mathrm{IF}}(t)$ and $f_{\mathrm{IF,ref}}(\mathrm{t})$ due to the diagnostic hardware can be minimized.

This goal is achieved by creating an “optimized” source frequency sweep, which is defined by the following con-

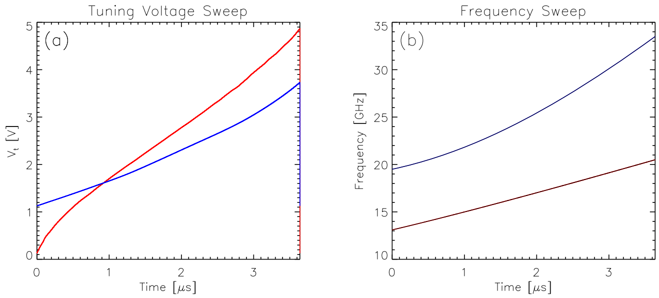

FIG. 6. (a) Tuning voltage sweeps for the $\mathrm{K_u}$-band (red) and the K-band (blue) systems using the iterative method, and (b) the corresponding optimized source frequency sweeps, overlayed on top of the analytic expressions (black) for $f(t)$ calculated from Eqs. 18 and 19.

dition:

$$f_{\mathrm{IF,ref}}(t) = \mathrm{constant} \equiv \mathcal{C}. \tag{16}$$

The tuning voltage waveform $V_{\mathrm{t}}(t)$, corresponding to the optimized sweep, is obtained through iterative correction to V_{t} using the IF signal phase (see Appendix A). The optimized frequency sweep eliminates the effect of systematic dispersion on $f_{\mathrm{IF,ref}}(t)$, as is shown in Fig. 5(b). We note that $\gamma(t)$ is no longer constant in time, as is shown in Fig. 5(c), and the equations for $\tau_{\mathrm{p}}(f)$ (Eq. 6), as well as $f_{\mathrm{IF,edge}}(t)$:

$$f_{\mathrm{IF,edge}}(t) = f_{\mathrm{IF,ref}}(t) - \frac{\ell_{\mathrm{ref}} - \ell_{\mathrm{vac}}}{c}\gamma(t), \tag{17}$$

must use this time-dependent form of $\gamma(t)$. Figure 5(d) shows that the values of $\tau_{\mathrm{p}}(f)$ from Eq. 6 are a good match to the original input values calculated for the model.

Figure 6(a) shows the tuning voltage sweeps for the $\mathrm{K_u}$- and K-bands determined using the iterative method, while Fig. 6(b) shows the corresponding optimized frequency sweeps. As a verification of the iterative method, an anlaytic expression for $f(t)$ can be derived (see Appendix B, Eq. B15) using the form of $\tau_{\mathrm{IF,ref}}(f)$ in Eq. 11, and the equations

$$t(f) = \frac{1}{\mathcal{C}} \int_{f_{\mathrm{start}}}^{f} \tau_{\mathrm{IF,ref}}(f')df' \tag{18}$$

$$\mathcal{C} = \frac{1}{T} \int_{f_{\mathrm{start}}}^{f_{\mathrm{end}}} \tau_{\mathrm{IF,ref}}(f')df', \tag{19}$$

where T is the time duration of the sweep and f_{start}, f_{end} are the lower and upper limits of the frequency. The expression in Eq. B15 we will designate as the ideal optimized source frequency sweep $f_{\mathrm{ideal}}(t)$; these curves are also shown in Fig. 6(b).

D. Deviations of $f(t)$ from $f_{\mathrm{ideal}}(t)$

In Sec. III.C, the tuning voltage, and consequently the frequency sweep, was iteratively modified to linearize $\phi_{\mathrm{IF,ref}}(t)$ (or to set $f_{\mathrm{IF,ref}}(t)$ = constant). The tuning voltage waveform is distorted to 1) counteract the non-linear $f(V_{\mathrm{t}})$ relation (see Fig. 7(a)), and 2) compensate for the group delay characteristics of the system. If the group delay is represented by Eq. 11, then iterative optimization of the frequency sweep will attempt to generate the smooth waveform given by Eq. B15 or $f_{\mathrm{ideal}}(t)$. With real world electronics $f_{\mathrm{ideal}}(t)$ cannot be completely eliminated. This effect has been discussed in detail in Ref. 7, where it was shown that a pattern in df/dV_{t} can appear as an artifact in the IF signal, which will grow with distance from the reference target position. The size of the artifacts can be reduced through various means, e.g., increasing the bandwidth of the V_{t} amplifier and using a waveform generator with a higher resolution.

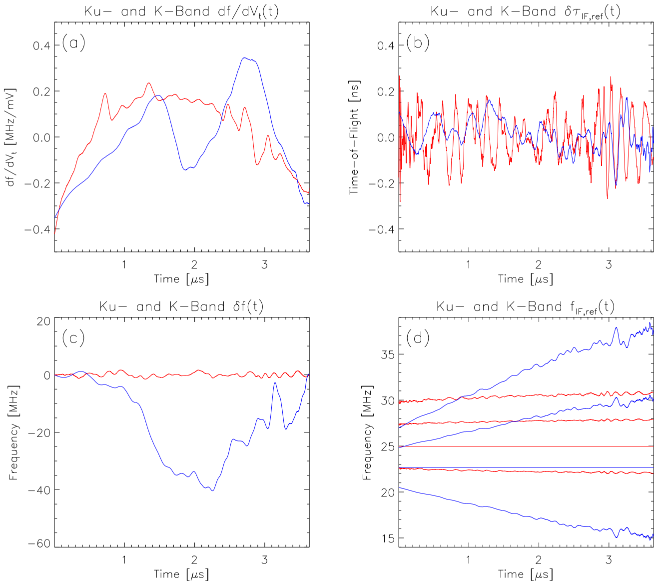

FIG. 7. (a) Variation of df/dV_{t} and $\delta\tau_{\mathrm{IF,ref}}(t)$ during the frequency sweep, where the constant and linear trends have been removed. Red indicates $\mathrm{K_u}$-band, while blue indicates K-band. (b) $\delta\tau_{\mathrm{IF,ref}}(t)$ or time dependence of deviation from the ideal group delay curve (Eq. 11 or the red curves in Figs. 4(c) and 4(d)). (c) and (d) show calculations based on the data shown in Fig. 7(b). (c) Corresponding deviation of the source frequency $\delta f(t)$ due to $\delta\tau_{\mathrm{IF,ref}}(t)$. (d) Variation of the IF signal frequency as the reference target is moved from its original position by $\Delta\ell$: from top to bottom, $\Delta\ell$=40, 20, 0, −20 cm.

On the other hand, if group delay ripples $\delta\tau_{\mathrm{IF,ref}}(t)$ are present in the system, then the optimization procedure will imprint an error $\delta f(t)$ onto $f(t)$. Figure 7(b) shows the ripple on $\tau_{\mathrm{IF,ref}}(f)$, defined as the difference between the experimental data and the best fit to Eq. 11, both shown in Figs. 4(c) and 4(d). This data can be used to estimate the error $\delta f(t)$ due to $\delta\tau_{\mathrm{IF,ref}}(f)$, as is shown in Fig. 7(c), while Fig. 7(d) plots the resulting $f_{\mathrm{IF,ref}}(t)$ for various target distances. We note that sharper changes in $\delta f(t)$ genearate larger variations in $f_{\mathrm{IF,ref}}(t)$, and that these artifacts grow as the distance from the reference target position is increased.

Appendix C explains how a perturbation $\delta f(t)$ can generate systematic errors (or artifacts) in $\Delta f_{\rm IF}(t)$. If $\delta f(t)$ is expressed in terms of a Fourier sine series with coefficients b_n, then the deviation in $\Delta f_{\rm IF}(t)$ due to $\delta f(t)$ can be written

$$\Delta\tilde{f}_{\rm IF}(t) \simeq -\sum_{n=1}^{\infty} 2b_n \sin\left\{\frac{n\pi}{T}\frac{\Delta\tau_{\rm IF}(t)}{2}\right\}\cos\left\{\frac{n\pi}{T}t\right\}, \tag{20}$$

where

$$\Delta\tau_{\rm IF}(t) = \tau_{\rm RF}(f_{\rm RF}(t)) - \tau_{\rm RF,ref}(f_{\rm RF,ref}(t)) \tag{21}$$

$$f_{\rm RF}(t) = f(t - \tau_{\rm RF}(f_{\rm RF}(t))) \tag{22}$$

$$f_{\rm RF,ref}(t) = f(t - \tau_{\rm RF,ref}(f_{\rm RF,ref}(t))). \tag{23}$$

Equation 20 shows that amplitude of the error term is dependent nonlinearly on both n and $\Delta\tau_{\rm IF}(t)$.

Due to the complex form of Eq. 20, correcting the IF signal post acquisition is extremely difficult, hence the following best practice is used for minimizing errors due to $\delta f(t)$: the reference target should be placed at a distance that generates a time delay that is equivalent to some median or average time delay from the plasma. For the case shown in Fig. 5(d), a TOF of 1.33 ns is equivalent to a reference distance of ~20 cm from the plasma edge R_a (or antenna edge $R_{\rm ant}$); this is also the location of our reference target in the previous sections.

IV. PROFILE RECONSTRUCTION

The reconstruction of the electron density profile is performed in two steps: 1) processing of the IF signal to generate $\tau_{\rm p}(f)$, and 2) inverting this data to generate range information $h(f)$, or its inverse function $f(h)$=$f_{\rm pe}(h)$, and equivalently $n_{\rm e}(h)$ in the case of O-mode polarization. Here h is the *true* distance from the plasma edge (as opposed to the virtual distance $h' = c\tau_{\rm p}$). Step 1) is facilitated by creating a radar image from the IF signals, and this process is outlined in Sec. IV.A. Step 2) utilizes the POLAN algorithm to perform least-squares fitting of true and virtual distance data to a model for the local variation of $h(f_{\rm pe})$. This procedure is outlined in Sec. IV.B.

A. Signal and Image Processing

Using the time series of the IF signal from each sweep, radar images of the two frequency bands are generated on a common grid with vertical and horizontal axes given by $n_{\rm e}[i]$ and $h'[j] = c\tau[j]$, respectively. Here i and j are the pixel indices, and for O-mode constant pixel dimensions ($\Delta n_{\rm e}$, $\Delta h' = c\Delta\tau_{\rm p}$ constant) can be achieved so that both axes are properly scaled. The radar image is a spectrogram of the IF signal using the short-time Fourier transform, where the i-th section of the signal or bin is localized around $f(t) = f_{\rm pe}(n_{\rm e}[i])$. Typically 50% overlap and a Hanning window are used.

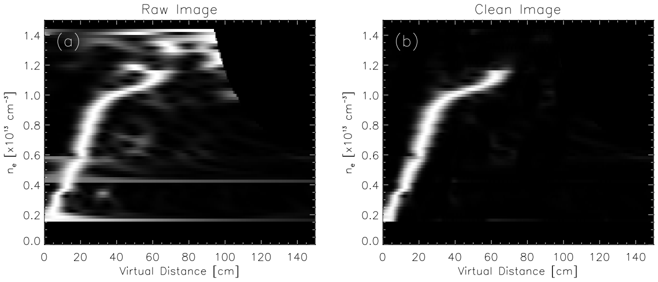

FIG. 8. (a) Raw radar image and (b) clean radar image after clutter has been removed.

The condition that the pixel dimensions are constant imposes signal processing conditions which are outlined in Appendix D. For this paper we used values of $c\Delta\tau_{\rm p}$=0.75 cm and either $\Delta n_{\rm e}$=1×10^{11} or 2×10^{11} cm^{-3}. Separate radar images for both freqency bands are generated on identical grids, with the origin of the horizontal axis coinciding with the edge of the antennas. These images are merged to form a single radar image with a vertical axis ranging from 0 to 1.5×10^{13} cm^{-3}.

Figure 8(a) shows an example of the raw radar image with pixel dimensions 201×76 (width×height). For better resolution, each row of pixels has been normalized by its peak value. In addition to the main reflection from the cutoff density, the radar image often contains clutter due to backscattering from fluctuations away from the cutoff density, as well as echos from multiple reflections between the cutoff layer and the shell. Figure 8(b) shows the same radar image after the clutter has been removed. The main advantage of generating radar images is that the quality of the data can be easily evaluated. Each image is stored as an 8-bit PNG file, which can be easily viewed by any graphical viewer application, or bundled as a movie. Another advantage is that the images can be easily cleaned or decluttered, either manually or automatically, using common image manipulation software such as Photoshop, GIMP, ImageMagick, etc.

Finally, each row of pixels provides an estimate of $\tau_{\rm p}(f[i])$ through weighted averaging using the image intensity. Here the horizontal pixel resolution $\Delta h'$ is smaller than the radar range resolution,[14,15] hence the weighted variance is used as an estimate of the uncertainty in the virtual height measurement $\pm\delta h'(f)$.

B. Density Profile Inversion Using POLAN

In order to obtain the true or real distance $h(f)$ to the cutoff position, $\tau_{\rm p}(f)$ must be inverted in accordance with Eqs. 1-3. The POLAN[13] algorithm combines several attractive features: 1) the flexibility of using either the O- or X-mode dispersion relation, or both simultaneously when data from both polarizations is available, and 2) regularization in the form of least squares fitting of the experimental data to a polynomial model, using both the true distances $h(f)$ and the reduced virtual distances $h''(f)$.

POLAN uses a lamination method to solve the forward problem for the virtual distance:

$$h'(f) = \int_0^{h(f)} \mu_{\mathrm{g}}(f, r)\, dr. \tag{24}$$

A polynomial model of order n_{t} for the true distance $h_{\mathrm{m}}(f)$ around an anchor point f_{a}:

$$h_{\mathrm{m}}(f) - h_{\mathrm{a}} = \sum_{j=1}^{n_{\mathrm{t}}} q_j (f - f_{\mathrm{a}})^j \tag{25}$$

generates the following estimate for the reduced virtual distance $h''_{\mathrm{m}}(f, f_{\mathrm{a}})$ for $f > f_{\mathrm{a}}$:

$$\begin{aligned} h''_{\mathrm{m}}(f, f_{\mathrm{a}}) - h_{\mathrm{a}} & \\ = \int_{h(f_{\mathrm{a}})}^{h(f)} \mu_{\mathrm{g}}(f, h) dh &= \int_{f_{\mathrm{a}}}^{f} \mu_{\mathrm{g}}(f, f') \frac{dh(f')}{df'} df' \\ &= \sum_{j=1}^{n_{\mathrm{t}}} q_j j \int_{f_{\mathrm{a}}}^{f} \mu_{\mathrm{g}}(f, f')(f' - f_{\mathrm{a}})^{j-1} df' \end{aligned} \tag{26}$$

For a set of real and virtual (i.e. inverted and experimental) data points around f_{a}, Eqs. 25 and 26 can be solved using weighted linear least squares to estimate the model coefficients q_j, j=1, …, n_{t}. Equation 25 is then used to generate the next real height data point f_{b} above f_{a}, which then becomes the new anchor point for the next iteration. We note that the remaining data points ($h''_{\mathrm{m}}(f, f_{\mathrm{a}})$ for $f > f_{\mathrm{b}}$) must also be adjusted to obtain a new set of reduced virtual distances, with f_{b} as the anchor point:

$$\begin{aligned} h''_{\mathrm{m}}(f, f_{\mathrm{b}}) = h''_{\mathrm{m}}(f, f_{\mathrm{a}}) &+ [h(f_{\mathrm{b}}) - h(f_{\mathrm{a}})] \\ &- \int_{h(f_{\mathrm{a}})}^{h(f_{\mathrm{b}})} \mu_{\mathrm{g}}(f, h) dh \\ = h''_{\mathrm{m}}(f, f_{\mathrm{a}}) &+ [h(f_{\mathrm{b}}) - h(f_{\mathrm{a}})] \\ - \sum_{j=1}^{n_{\mathrm{t}}} q_j j &\int_{f_{\mathrm{a}}}^{f_{\mathrm{b}}} \mu_{\mathrm{g}}(f, f')(f' - f_{\mathrm{a}})^{j-1} df'. \end{aligned} \tag{27}$$

For the analyses shown in this paper, a value of n_{t}=3 and four virtual points are used in addition to a single real point, with weights inversely proportional to both $\delta h'(f)$ and $|f - f_{\mathrm{a}}|$. Two edge points, i.e. $h(f[0]{=}0)$ and $h(f[1])$, are specified and serve as starting points for the density profile reconstruction. The antenna position is used for R_a(=R_{ant}, hence $h(f[0])$=0), while $h(f[1])$ is linearly interpolated from the origin to the virtual height of the first data point. Errors due to different initialization methods for O-mode profile reconstruction have been examined in detail elsewhere.[16,17] We note that with POLAN, a very simple edge model (specification of two points in our case) will still generate a smooth profile that is consistent with the available data. At the upper limit of the profile, real points are substituted for virtual points so that the total number of data points used in the least squares fitting is kept constant at five. The value of R_{ant} is referenced from the surface of the centerstack, using the TOF of reflections during vacuum shots. Examples of reconstructed density profiles are shown in Figs. 11 and 12.

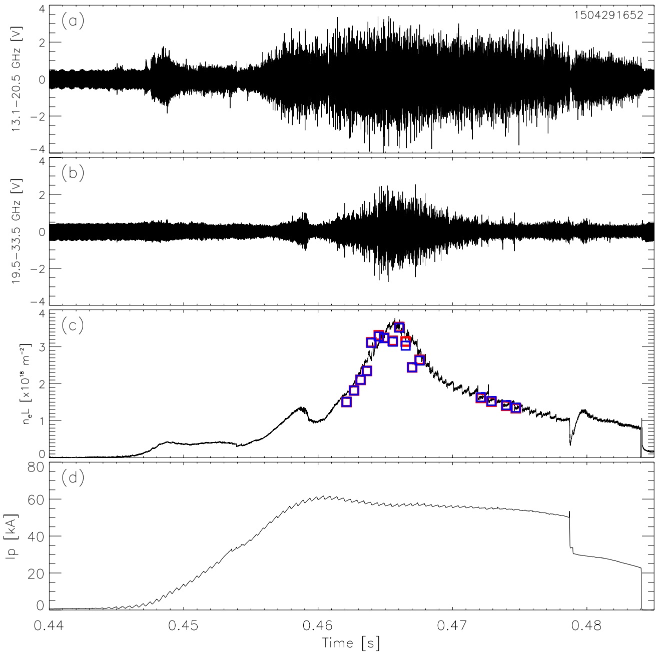

FIG. 9. (a) and (b) show the reflectometer raw signals, while (c) shows the line density. Also shown are line densities calculated using the LFS reflectometer profiles and LRDFIT equilibria used to map the HFS. Red squares show the case where missing portion of the density profile in the region near R_{m} are interpolated, while blue squares show the case where the density is assumed to be flat. (d) shows the evolution of the plasma current.

V. FM-CW MEASUREMENTS ON LTX

A. Raw Signals

The measurements presented here were made for discharges on LTX with B_T = 1.6 kG and I_P = 60 kA. Examples of the raw signals and the line density evolution are shown in Fig. 9. The electron cyclotron frequency at the edge is ∼3 GHz, hence the advantages of using X-mode polarization are limited. For this work, O-mode polarization for the launch/receive antennas was used exclusively (E-plane of antennas is tilted ∼10° from horizontal, nominal magnetic pitch angle at edge is ∼15°).

Examples of the raw IF signals from the two bands

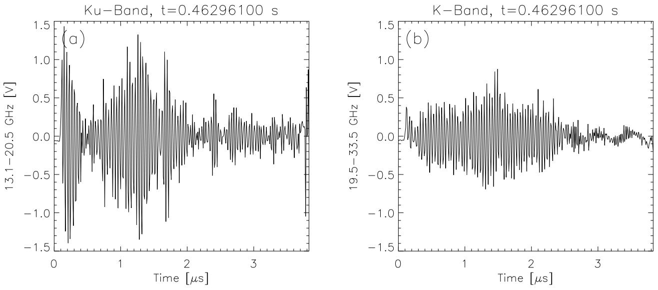

FIG. 10. (a) and (b) show the K_u-band and K-band IF signals, respectively, for a single frequency sweep.

for an individual frequency sweep can be seen in Figs. 10(a) and (b). Due to the horizontal orientation of the launch and receive antennas, both signals display a strong reflection from the center stack above the peak cutoff frequency. The amplitude of the IF signals can exhibit strong variations due to deflection or scattering by fluctuations.

B. Electron Density Profiles

The steep rise in the line density near the plasma current peak is initiated by a large gas puff at 0.460 s. Subsequently, the line density drops to about a third of its peak value by ∼0.475 s, hence it is important to evaluate the performance of the reflectometer in these two regimes (high and low density). Examples of the reconstructed electron density profile are shown in Figs. 11 and 12 for the high (t=0.467 s) and low (t=0.474 s) density portions of the discharge, respectively. It should be noted that a pixel resolution of Δn_e=2×10^{11} cm^{-3} was used for the high density case, while a higher pixel resolution of Δn_e=1×10^{11} cm^{-3} was required for the low density case, in order to better resolve the shape of $\tau_\mathrm{p}(f)$ (and $n_\mathrm{e}(h)$). Figures 11(a) and 12(a) show ten individual profiles that are sampled 8 μs apart. Profiles generated from the average of all of the radar images and the corresponding uncertainties using $\pm\delta h'(f)$ are also shown.

Figures 11(b) and 12(b) compare the averaged profiles with Thomson scattering (TS) measurements. It should be clarified that the single-pulse TS diagnostic is used to create n_e and T_e profiles for an average discharge, and that the final density profiles were normalized using the interferometer line dnesity. For the high density case, the missing portion of the reflectometer data below n_e=2.2×10^{12} cm^{-3} comprises only a small fraction of the density profile; good agreement with TS is achieved even close to the plasma edge. For the low density case, data from about half of the density profile is missing. Our simple guess for the initial edge points still generates profiles that are consistent with the TS measurements where the data overlap.

The reflectometer results were also compared to the interferometer measurements by generating line densities using the reflectometer profiles and magnetic equilibrium reconstructions. The poloidal flux function generated by LRDFIT[18] (LR circuit model with Data FITting capabilities) was used to map the low-field side (LFS) density profile to the high-field side (HFS). If the core profile is flat or the peak density is too high, the reflectometer profiles will not fully extend to the magnetic axis. In these situations the missing section was either interpolated or assumed to be flat. The results from both cases are shown in Fig. 9(c) for several time slices coinciding with the LRDFIT calculations. Values of the reflectometer line density track closely with the interferometer measurements prior to the line density peak. Near the peak, values calculated from the reflectometer data begin to show larger scatter and deviation from the interferometer measurements. Here the core density rises above the maximum cutoff density of the reflectometer, and the start of sawtooth activity may introduce strong radial variations in the profile shape, as well in-board/outboard asymmetry. The reflectometer calculations remain within 15% of the interferometer line densities in the high density phase of the discharge, while they are within 5% during the low density phase.

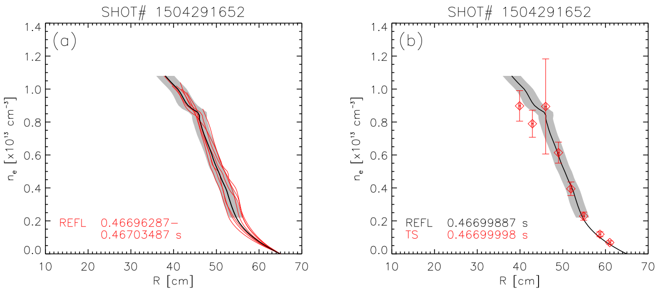

FIG. 11. Reconstructed electron density profiles for the high density case (t=0.467 s) (a) Ten individual profiles (red) at 8 μs intervals. Overlayed is the mean profile (black) and measurement uncertainty (gray) generated from the average of the radar images. (b) Mean reflectometer profile and uncertainty compared to Thomson scattering (red diamonds).

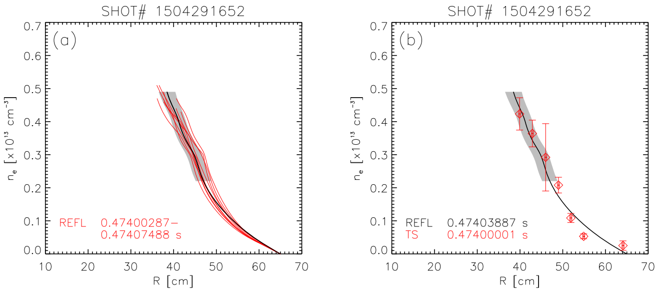

FIG. 12. Reconstructed electron density profiles for the low density case (t=0.474 s). (a) Ten individual profiles (red) at 8 μs intervals. Overlayed is the mean profile (black) and measurement uncertainty (gray) generated from the average of the radar images. (b) Mean reflectometer profile and uncertainty compared to Thomson scattering (red diamonds).

VI. FUTURE HARDWARE UPGRADES AND ANALYSES

Measurements of fluctuations will be of key interest in the upgraded LTX-β device, which will feature higher B_T and I_P, and neutral beam heating. Enhancements to the FM-CW reflectometer are will improve the capability of the system to function as fluctuation diagnostic.

A GaGe CompuScope 1242 digitizer will add four additional data acquisition channels, which will allow sampling of the two IF2 signals as well as the monitor signals for the tuning voltages. The data acquisition can then be run continuously instead of in burst mode (triggered), which will decrease the time interval between sweeps to 4 μs.

A second advantage is that the additional signals can be used to eliminate timing uncertainties between the microwave frequency sweep and the IF signals. The complex amplitude of the IF signal can then be extracted at set frequencies, similar to fixed-frequency quadrature reflectometer systems.[19] As explained in Sec. IV, inherent resolution limits exist for measurements of density fluctuations using the profile reconstruction technique. Access to phase and amplitude measurements will allow better estimates of the spatial structure of low-k fluctuations. The complex amplitude signals can also be used with radial correlation techniques for turbulence correlation length estimates.[20]

Finally, the radar image itself is a good tool for looking at fluctuations. For low-k perturbations atop the density profile, local variations in the density gradient will introduce strong inflections in the virtual distance. For high-k (up to 16 cm^{-1}), reflections due to radial backscattering will introduce peaks in the radar image at locations away from the cutoff layer.

ACKNOWLEDGMENTS

The authors would like to thank T. Holoman for constructing the support stand for the jacking stage and bellows. This work was supported by U.S. Department of Energy Contracts DE-AC02-09CH11466 and DE-FG02-99ER54527.

Appendix A: Iterative Determinatinon of $V_\mathrm{t}(t)$ for the Optimized $f(t)$

The reference target is a metal plate in front of a mockup of the waveguide and antenna sections of the vacuum interface. The waveguide to coaxial adapters are transferred from the vacuum interface to the mockup, while the rest of the diagnostic remains *in situ*. Identical data acquisition and trigger rates are used as during experiments (10,000 records, 8 μs trigger interval, 100 MSa/s sampling rate) to account for the dynamic response of the electronics. The f–V_t static calibration results from Sec. III.B are used to generate the an initial V_t waveform (e.g. a linear frequency sweep). The following steps are then used for creating the tuning voltage waveform for the optimized source frequency sweep:

1. Load the tuning voltage waveform $V_\mathrm{t}[j]$, $j = 0, \ldots, N-1$ ($N = 64$ kpoints) into the AWG memory.
2. Trigger AWG and data acquisition.
3. FFT interpolate each record to 8× the original sample rate. Average multiple records to generate an interpolated "clean" IF signal.
4. Determine the accumulated phase $\phi_{\mathrm{IF,ref}}(t)$ of the IF signal. Obtain the phase deviation $\Delta\phi_{\mathrm{IF,ref}}(t)$ from a linear phase ramp $\overline{\phi}_{\mathrm{IF,ref}}(t)$:
$$\overline{\phi}_{\mathrm{IF,ref}}(t) = \phi_{\mathrm{IF,ref}}(T)\frac{t}{T} \tag{A1}$$
$$\Delta\phi_{\mathrm{IF,ref}}(t) = \phi_{\mathrm{IF,ref}}(t) - \overline{\phi}_{\mathrm{IF,ref}}(t). \tag{A2}$$
5. Introduce an attenuation factor $A \leq 1$ to generate a new IF signal phase $\phi'_{\mathrm{IF,ref}}(t)$:
$$\phi'_{\mathrm{IF,ref}}(t) = \overline{\phi}_{\mathrm{IF,ref}}(t) + A\Delta\phi_{\mathrm{IF,ref}}(t). \tag{A3}$$
6. Resample the equi-spaced time axis t to a new time axis t' that generates a linear $\phi'_{\mathrm{IF,ref}}(t')$. The orginal V_t array with time axis t' is interpolated back to an equi-spaced time axis t to create a new tuning voltage sweep V'_t.
7. Generate a 12-bit integer signal (64 kpoint wide array) from $V'_\mathrm{t}(t)$ to load to AWG memory.

These steps are repeated until $|\Delta\phi_{\mathrm{IF,ref}}(t)|_{\max}$ is minimized. For a value $A = 0.5$, this typically requires 3 to 4 iterations.

Appendix B: Analytic Expressions for the Optimized $f(t)$ and $\gamma(t)$

Assume that $\mathcal{C}$ and T are specified, and that $\tau_{\mathrm{IF,ref}}(f)$ are known for an array of values f with range $[f_{\mathrm{start}}, f_{\mathrm{end}}]$. For a dispersionless LO path, we can write the following relations:

$$t_{\mathrm{LO}}(f) = t(f) + \tau_{\mathrm{LO}} \tag{B1}$$
$$t_{\mathrm{LO}}(f + \mathcal{C}) = t_{\mathrm{RF,ref}}(f) \tag{B2}$$
$$\tau_{\mathrm{IF,ref}}(f) = t_{\mathrm{RF,ref}}(f) - t_{\mathrm{LO}}(f). \tag{B3}$$

Here $t_{\mathrm{LO}}(f)$ and $t_{\mathrm{RF,ref}}(f)$ indicate the time from the beginning of the sweep when the wave component with frequency f reaches the mixer along the LO and RF paths, respectively, while $t(f)$ represents the source frequency sweep (inverse equation of $f(t)$).

Equations B1–B3 can be used to write the differential equation

$$\frac{dt(f)}{df} \simeq \frac{t(f+\mathcal{C}) - t(f)}{\mathcal{C}} = \frac{\tau_{\mathrm{IF,ref}}(f)}{\mathcal{C}}, \tag{B4}$$

which yields an integral expression for $t(f)$:

$$t(f) = \frac{1}{\mathcal{C}} \int_{f_{\mathrm{start}}}^{f} \tau_{\mathrm{IF,ref}}(f')df' \tag{B5}$$

$$\mathcal{C} = \frac{1}{T} \int_{f_{\mathrm{start}}}^{f_{\mathrm{end}}} \tau_{\mathrm{IF,ref}}(f')df'. \tag{B6}$$

Analytic expressions for Eqs. B5 and B6 can be found by using

$$\tau_{\mathrm{IF,ref}}(x) = a + bx, \tag{B7}$$

where coefficients a and b were determined in Sec. III.B from the best fit curve to the experimental data, and have the definitions

$$a = \frac{\ell_{\mathrm{RF,coax}} - \ell_{\mathrm{LO,coax}}}{v_{\mathrm{g,coax}}} + \frac{\ell_{\mathrm{ref}}}{c}, \quad b = \frac{\ell_{\mathrm{wg}}}{c}. \tag{B8}$$

The variable x is expressed in terms of f and the waveguide cutoff frequency f_{c} as

$$x^2 = \frac{c^2}{v_{\mathrm{g,wg}}^2(f)} = \frac{f^2}{f^2 - f_{\mathrm{c}}^2}, \tag{B9}$$

from which we can write

$$f^2 = f_{\mathrm{c}}^2 \frac{x^2}{x^2-1}, \quad \frac{df}{dx} = -\frac{f_{\mathrm{c}}}{(x^2-1)^{3/2}}. \tag{B10}$$

Equation B5 can now be written

$$\begin{aligned} t(x) &= \frac{1}{\mathcal{C}} \int_{x(f_{\mathrm{start}})}^{x(f)} \tau(x') \frac{df}{dx'} dx' \\ &= -\frac{1}{\mathcal{C}} \int_{x_{\mathrm{start}}}^{x} (a + b\,x') \frac{f_{\mathrm{c}}}{(x'^2-1)^{3/2}} dx' \\ &= \frac{f_{\mathrm{c}}}{\mathcal{C}} \frac{a\,x' + b}{\sqrt{x'^2-1}} \bigg|_{x_{\mathrm{start}}}^{x}, \end{aligned} \tag{B11}$$

and similarly for Eq. B6

$$\mathcal{C} = \frac{f_{\mathrm{c}}}{T} \frac{a\,x' + b}{\sqrt{x'^2-1}} \bigg|_{x_{\mathrm{start}}}^{x_{\mathrm{end}}}. \tag{B12}$$

In terms of f these equations have the following form:

$$t(f) = \frac{1}{\mathcal{C}} \left[af' + b\sqrt{f'^2 - f_{\mathrm{c}}^2} \right] \bigg|_{f_{\mathrm{start}}}^{f} \tag{B13}$$

$$\mathcal{C} = \frac{1}{T} \left[af' + b\sqrt{f'^2 - f_{\mathrm{c}}^2} \right] \bigg|_{f_{\mathrm{start}}}^{f_{\mathrm{end}}}. \tag{B14}$$

Equation B13 can also rewritten as a function $f(t)$ to give an analytic expression for the optimized source frequency sweep:

$$f(t) = \frac{1}{(a^2-b^2)} \Big[a\,(\mathcal{D} + \mathcal{C}t) - b\sqrt{(b^2-a^2)f_{\mathrm{c}}^2 + (\mathcal{D}+\mathcal{C}t)^2} \Big] \tag{B15}$$

and

$$\gamma(t) = \frac{\mathcal{C}}{(a^2-b^2)} \left[a - \frac{b(\mathcal{D}+\mathcal{C}t)}{\sqrt{(b^2-a^2)f_{\mathrm{c}}^2 + (\mathcal{D}+\mathcal{C}t)^2}} \right], \tag{B16}$$

where

$$\mathcal{D} \equiv af_{\mathrm{start}} + b\sqrt{f_{\mathrm{start}}^2 - f_{\mathrm{c}}^2}. \tag{B17}$$

Appendix C: FM-CW Radar with Oscillating $\delta f(t)$

Let us write the source frequency as

$$f(t) = f_{\mathrm{ideal}}(t) + \delta f(t), \tag{C1}$$

where $f_{\mathrm{ideal}}(t)$ is the ideal portion of the optimized frequency sweep (cf. Eq. B15) and $\delta f(t)$ represents a small oscillating component such as ripple. If $\delta f(t)$ is expressed in terms of the Fourier sine series

$$\delta f(t) = \sum_{n=1}^{\infty} b_n \sin\left(\frac{n\pi t}{T}\right) \tag{C2}$$

with coefficients

$$b_n = \frac{2}{T} \int_0^T \delta f(t) \sin\left(\frac{n\pi t}{T}\right) dt, \tag{C3}$$

then the frequency of the IF signals can be written

$$f_{\mathrm{IF,ref}}(t) = f_{\mathrm{ideal}}(t') - f_{\mathrm{ideal}}(t' - \tau'_{\mathrm{IF,ref}}(t)) + \sum_{n=1}^{\infty} 2b_n \sin\left\{\frac{n\pi}{T}\frac{\tau'_{\mathrm{IF,ref}}(t)}{2}\right\} \cos\left\{\frac{n\pi}{T}\left[t' - \frac{\tau'_{\mathrm{IF,ref}}(t)}{2}\right]\right\} \tag{C4}$$

$$f_{\mathrm{IF}}(t) = f_{\mathrm{ideal}}(t') - f_{\mathrm{ideal}}(t' - \tau'_{\mathrm{IF}}(t)) + \sum_{n=1}^{\infty} 2b_n \sin\left\{\frac{n\pi}{T}\frac{\tau'_{\mathrm{IF}}(t)}{2}\right\} \cos\left\{\frac{n\pi}{T}\left[t' - \frac{\tau'_{\mathrm{IF}}(t)}{2}\right]\right\}, \tag{C5}$$

where $t' = t - \tau_{\mathrm{LO}}(f_{\mathrm{LO}}(t))$ and

$$\tau'_{\mathrm{IF,ref}}(t) = \tau_{\mathrm{RF,ref}}(f_{\mathrm{RF,ref}}(t)) - \tau_{\mathrm{LO}}(f_{\mathrm{LO}}(t)) \tag{C6}$$

$$\tau'_{\mathrm{IF}}(t) = \tau_{\mathrm{RF}}(f_{\mathrm{RF}}(t)) - \tau_{\mathrm{LO}}(f_{\mathrm{LO}}(t)). \tag{C7}$$

We also have the following definitions:

$$f_{\mathrm{LO}}(t) = f(t') \tag{C8}$$

$$f_{\mathrm{RF,ref}}(t) = f(t' - \tau'_{\mathrm{IF,ref}}(t)) \tag{C9}$$

$$f_{\mathrm{RF}}(t) = f(t' - \tau'_{\mathrm{IF}}(t)). \tag{C10}$$

With Eqs. C4 and C5, $\Delta f_{\rm IF}$ (cf. Eq. 6) has the form

$$\Delta f_{\rm IF}(t) = f_{\rm ideal}(t'') - f_{\rm ideal}(t'' - \Delta\tau_{\rm IF}(t)) \\ -\sum_{n=1}^{\infty} 2b_n \sin\left\{\frac{n\pi}{T}\frac{\Delta\tau_{\rm IF}(t)}{2}\right\} \cos\left\{\frac{n\pi}{T}\left[t'' - \frac{\Delta\tau_{\rm IF}(t)}{2}\right]\right\}, \tag{C11}$$

with $t'' = t - \tau'_{\rm RF,ref}(t)$ and

$$\Delta\tau_{\rm IF}(t) = \tau_{\rm RF}(f_{\rm RF}(t)) - \tau_{\rm RF,ref}(f_{\rm RF,ref}(t)). \tag{C12}$$

The final term in Eq. C11 represents deviations in $\Delta f_{\rm IF}(t)$ due to $\delta f(t)$, which has a maximum value for a given n:

$$2b_n \sin\left\{\frac{n\pi}{T}\frac{\Delta\tau_{\rm IF}(t)}{2}\right\} \simeq b_n n\pi \frac{\Delta\tau_{\rm IF}(t)}{T}, \tag{C13}$$

where the last approximation can be made for $\Delta\tau_{\rm IF}(t) \ll T$. Equation C13 reveals that the deviation for a given n is proportional to $\Delta\tau_{\rm IF}(t)$, and that higher-order (larger n) contributions to $\delta f(t)$ will have a larger effect. In addition, we see that Eq. C13 is inversely proportional to T, hence errors to $\Delta f_{\rm IF}(t)$ will be larger for faster sweeps.

Appendix D: Conditions for Radar Image with Constant Pixel Resolution

The spectrogram of the signal $\Delta f_{\rm IF}(t)$ can be plotted as an image with $f(t)$ (or $n_{\rm e}(f(t))$) and $\tau_{\rm p}$ (or $h' = c\tau_{\rm p}$) as the axes. The size of each data bin influences the pixel resolution along the two axes. The relationship between the signal processing parameters and the pixel resolution of the radar image $(\Delta n_{\rm e}, c\Delta\tau_{\rm p})$ are derived here for the case of O-mode polarization.

If we define for the i-th bin:

$$\Delta f[i] \equiv f[i+1] - f[i], \quad \Delta n_{\rm e}[i] \equiv n_{\rm e}[i+1] - n_{\rm e}[i], \tag{D1}$$

where we have the relation

$$f^2 = \frac{e^2}{\pi m_{\rm e}} n_{\rm e} = \frac{e^2 n_0}{\pi m_{\rm e}}\frac{n_{\rm e}}{n_0} \quad \text{or} \quad n_{\rm e} = \frac{n_0}{f_0^2} f^2, \tag{D2}$$

the pixel resolution for the cutoff density can be expressed as

$$\Delta n_{\rm e}[i] = \frac{n_0}{f_0^2}\left(f^2[i+1] - f^2[i]\right) \approx \frac{n_0}{f_0^2} 2f[i]\Delta f[i], \tag{D3}$$

where the last approximation holds for $f[i] \gg \Delta f[i]$. Here $f_0^2 = e^2 n_0/\pi m_{\rm e}$ is the square of the cutoff frequency for density n_0. Since the frequency resolution of the i-th bin is $f_{\rm s}/N_{\rm bin}[i]$, where $f_{\rm s}$ is the digitizer sampling rate, we can express the pixel resolution of the time-of-flight as

$$\Delta\tau_{\rm p}[i] = \frac{f_{\rm s}}{N_{\rm bin}[i]\gamma[i]}. \tag{D4}$$

Here let us set $\Delta n_{\rm e}[i] = \Delta n_{\rm e}$ as a constant, and choose $N_{\rm bin}[i]$ as an independent parameter (adjusted by zero-padding) that keeps $\Delta\tau_{\rm p}[i] = \Delta\tau_{\rm p}$ constant. Then from Eq. D4 we can obtain the formula for $N_{\rm bin}[i]$:

$$N_{\rm bin}[i] = \frac{f_{\rm s}}{\Delta\tau_{\rm p}\gamma[i]}. \tag{D5}$$

[1] E. Mazzucato, *Electromagnetic Waves for Thermonuclear Fusion Research* (World Scientific, Singapore, 2014).

[2] C. Laviron, A. J. H. Donné, M. E. C. Manso, J. Sanchez, Plasma Phys. Control. Fusion **38**, 905 (1996).

[3] K. Bibl, Ann. Geofis. **41**, 667 (2000).

[4] E. J. Doyle, T. L. Rhodes, W. A. Peebles, and L. Zeng, Rev. Sci. Instrum. **70**, 1064 (1999).

[5] V. L. Ginzburg, *The Propagation of Electromagnetic Waves in Plasmas, 2e* (Pergamon Press, Oxford, 1970).

[6] D. G. Swanson, *Plasma Waves, 2e* (Institute of Physics, London, 2003).

[7] T. Tokuzawa, A. Mase, N. Oyama, Y. Kogi, N. Goto, L. G. Bruskin, Rev. Sci. Instrum. **70**, 1068 (1999).

[8] S. Kubota, W. A. Peebles, X. V. Nguyen, N. A. Crocker, A. L. Roquemore, Rev. Sci. Instrum. **77**, 10E926 (2006).

[9] R. Majeski et al., Nuclear Fusion **49**, 055014 (2009).

[10] S. Kubota, X. V. Nguyen, W. A. Peebles, L. Zeng, E. J. Doyle, A. L. Roquemore, Rev. Sci. Instrum. textbf72, 348 (2001).

[11] T. Tokuzawa, A. Mase, N. Oyama, A. Itakura, T. Tamano, T, Rev. Sci. Instrum. **68**, 443 (1997).

[12] D. M. Pozar, *Microwave Engineering, 4e* (John Wiley & Sons, Hoboken, 2012).

[13] J. E. Titheridge, Radio Sci. **23**, 831 (1988).

[14] E. J. Doyle, K. W. Kim, J. H. Lee, W. A. Peebles, C. L. Rettig, T. L. Rhodes, R. T. Snider, in *Diagnostics for Experimental Thermonuclear Fusion Reactors*, Plenum Press, 117 (1996).

[15] E. J. Doyle, N. L. Bretz, K. W. Kim, W. A. Peebles, T. L. Rhodes, in *Diagnostics for Experimental Thermonuclear Fusion Reactors*, Plenum Press, 119 (1998).

[16] P. E. Varela, M. E. Manso, A. Silva, J. Hernandes, F. Silva, Rev. Sci. Instrum. **66**, 4937 (1995).

[17] M. Manso, L. Cupido, G. Leclert, D. Wagner, G. Vayakis, A. Donn'e, L. de Kock, C. Laviron, J. Sanchez, F. Serra, A. Silva, C. Walker, ITER Joint Central Team and EU Home Teams, in *Diagnostics for Experimental Thermonuclear Fusion Reactors*, Plenum Press, 139 (1998).

[18] http://nstx-u.pppl.gov/software/lrdfit

[19] N. A. Crocker, W. A. Peebles, S. Kubota, J. Zhang, R. E. Bell, E. D. Fredrickson, N. N. Gorelenkov, B. P. LeBlanc, J. E. Menard, M. Podestà, Plasma Phys. Control. Fusion **53**, 105001 (2011).

[20] B. Kurzan, S. de Peña Hempel, E. Holzhauer, B. D. Scott, F. Serra, W. Suttrop, A. Zeiler, ASDEX Upgrade Team, Plasma Phys. Control. Fusion **42**, 237 (2000).